Machine-Learning-Backed Evolutionary Exploration of Ti-rich SrTiO$_3$(110) Surface Reconstructions

Ralf Wanzenböck,[†] Esther Heid,[†] Michele Riva,[‡] Giada Franceschi,[‡] Alexander M. Imre,[‡] Jesús Carrete,[¶] Ulrike Diebold,[‡] and Georg K. H. Madsen[*,†]

[†]Institute of Materials Chemistry, TU Wien, A-1060 Vienna, Austria

[‡]Institute of Applied Physics, TU Wien, A-1040 Wien, Austria

[¶]Instituto de Nanociencia y Materiales de Aragón, CSIC-Universidad de Zaragoza, 50009 Zaragoza, Spain

E-mail: georg.madsen@tuwien.ac.at

Abstract

The investigation of inhomogeneous surfaces, where various local structures co-exist, is crucial for understanding interfaces of technological interest, yet it presents significant challenges. Here, we study the atomic configurations of the $(2 \times m)$ Ti-rich surfaces at (110)-oriented SrTiO$_3$ by bringing together scanning tunneling microscopy and transferable neural-network force fields combined with evolutionary exploration. We leverage an active learning methodology to iteratively extend the training data as needed for different configurations. Training on only small well-known reconstructions we are able to extrapolate to the complicated and diverse overlayers encountered in different regions of the heterogeneous SrTiO$_3$(110)-$(2\times m)$ surface. Our machine-learning-backed approach generates several new candidate structures, in good agreement with experiment and verified using density functional theory.

1

Introduction

In recent years, the application of machine-learned force fields (MLFFs) to materials discovery and structure exploration has markedly increased. Method development and their applications have been advancing in parallel, with innovative and powerful models synergizing with established and proven methods. For example, moving from neural-network force fields that utilize precomputed invariant descriptors[1–3] to adopting equivariant message passing networks[4–6] has enabled more data-efficient and transferable MLFFs. Modern applications include foundation models trained on a wide range of materials,[7] transferable water potentials,[8] and condensed phase chemistry.[9]

Here, we utilize MLFFs to explore the surface reconstructions of strontium titanate ($SrTiO_3$). This material exemplifies the richness of bulk, surface, and interface properties that can be accessed within a single perovskite material: Donor doping by chemical impurities,[10,11] oxygen vacancies,[10,12,13] or field effects[11,14] can turn it into an insulator, a metal, a superconductor or even induce confined metallic behaviour in the form of 2D electron gases. The diversity extends to the atomistic details of the surface,[15] where a variety of composition-related, polarity-compensating reconstructions have been found for the (001), (110) and (111) orientations.[16–23] It is known that specific $SrTiO_3$ surface reconstructions are difficult to reproduce and can depend on sample history and preparation conditions.[15] Notably, scanning tunneling microscopy (STM) studies of $SrTiO_3$ surfaces frequently reveal the coexistence and even intermixing of multiple surface structures,[17,22,24] a feature common to the surfaces of other complex perovskites such as $BaTiO_3$ and $(La,Sr)MnO_3$.[25,26] The variety of coexisting surface reconstructions and their dependence on sample history underlines the necessity of changing the framing from identifying a single specific reconstruction to mapping out the range of possible reconstructions. This diversity can serve as an ideal showcase of the power of MLFF-supported stochastic searches.

In particular, the enhanced accuracy and reliability of MLFFs facilitate the application of stochastic algorithms for structural exploration of materials.[27–32] Stochastic approaches

require a substantial volume of calculations and are impracticable with ab-initio methods such as density functional theory (DFT) as the backend. This holds especially true for large and complex systems, such as surface reconstructions of multi-element compounds. Such systems usually feature a complex energy surface with too many degrees of freedom to explore exhaustively, as well as many local minima, where local searches for an optimal structure largely depend on the initial geometry of the search. Given that stochastic searches produce more diverse structures than, e.g., molecular dynamics, a transferable, robust, and generalizable force field trained on a diverse dataset is key to their success.

An accurate MLFF is, however, just one part of the toolbox necessary to build a robust and efficient workflow for structure searches. The design of an MLFF can enhance or restrict its transferability and any MLFF has the potential to emit infinitely diverse mispredictions. This is especially significant for stochastic searches, which, by design, tend to move into regions that the model was not trained on. Extrapolation happens almost surely in high-dimensional models,[33] and therefore is not, by itself, an indicator of poor performance. Research has hence focused on estimates of uncertainty as proxies for the error incurred by using a given MLFF.[34–38] When that error is suspected to exceed tolerable margins, retraining with an expanded training set can help extend the applicability of the MLFF. In such scenarios, an efficient algorithm must aim toward issuing only as many ab-initio calculations as required, while preventing waste of resources on redundant or irrelevant configurations.[39,40] Thus, the need for an uncertainty metric to evaluate the quality of the results dovetails with the usefulness of such metrics for identifying or even generating optimally informative new configurations.[29] This makes stochastic structure searches naturally part of the domain of application of active learning (AL) workflows, where an informed data selection is achieved through uncertainty estimation.[41]

This work focuses on the less well-understood Ti-rich surface reconstructions at the (110) orientation of $SrTiO_3$. Literature describes numerous composition-related surface reconstructions that can be broadly grouped into two families, characterized by Ti-poor ($n \times 1$) and

3

https://doi.org/10.26434/chemrxiv-2024-9l6jc ORCID: https://orcid.org/0000-0001-9844-9145 Content not peer-reviewed by ChemRxiv. License: CC BY 4.0

Ti-rich $(2 \times m)$ overlayers on an otherwise unchanged bulk.[22] Here, n and m denote the number of (1×1) bulk unit cells covered in the [001] and [$\bar{1}$10] directions, respectively. Figure 1 shows examples of both variations. Ti-rich overlayers pose the particular challenge that, even when the Ti-to-Sr ratio is controlled,[22] numerous reconstructions lacking corresponding DFT models can coexist. Here, we again observe pronounced heterogeneity in new STM measurements and are able to identify varied reconstructions (see Fig. S1 of the SI). We mitigate the lack of suitable atomistic models of such heterogeneous surfaces by combining an evolutionary search algorithm with a transferable MLFF to identify valid candidate structures. Transferability, in particular, is an important prerequisite for minimizing the computational cost associated with generating training data. We demonstrate that by utilizing small, well-known reconstructions and implementing a careful data selection routine built on structural and spatially-resolved local uncertainties, we can arrive at an MLFF capable of extrapolating to larger, more complex structures. In the following, we first discuss the active learning approach. We then proceed to show how structural models reproducing the STM images can be systematically obtained for all the coexisting surface structures.

Results and discussion

Active learning workflow for initial dataset

We set out to iteratively construct a versatile MLFF, which can subsequently be used in combination with an evolutionary search, specifically the covariance matrix adaptation evolution strategy (CMA-ES),[42] to explore different unit cells of the Ti-rich $SrTiO_3(110)$ surface. Due to the complex nature of the various surface reconstructions, the MLFF must be capable of resolving a wide range of local environments. Additionally, given the nature of the ES, which produces more diverse and possibly unphysical structures than, e.g., molecular dynamics, intermediate configurations are likely to exhibit unusual properties, such as unphysical bond lengths. For that reason, the MLFF needs to be robust and the underlying training data

4

diverse, making the construction of a suitable training set containing ab-initio energies and forces far from trivial. Furthermore, we aim to explore (2×5) surface reconstructions with up to 450 atoms per unit cell where the computational costs associated with DFT evaluation is prohibitive for constructing diverse training databases. The MLFF must therefore also be able to generalize from smaller training structures to the larger unit cells explored.
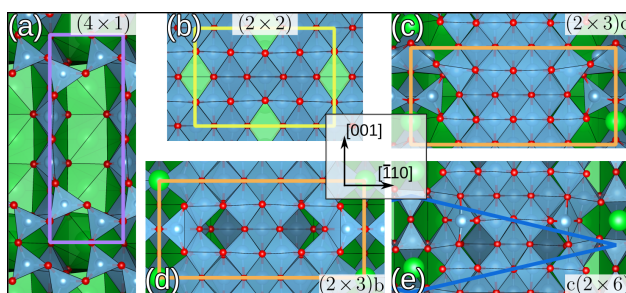

Figure 1: Top view of $SrTiO_3(110)$-$(n \times m)$ surface reconstructions: previously explored (4×1),[18] (2×2) and (2×3)b,[21] and newly identified (2×3)c and c(2×6) from this work. O atoms are shown in red, Sr in green and Ti in blue. The blue polyhedra depict TiO_4 tetrahedra in the first subplot (panel a) and, predominantly, TiO_6 octahedra in the others. Each unit cell is marked by colored lines. $(n \times 1)$ overlayers exclusively contain tetrahedrally coordinated TiO_4 units, while $SrTiO_3(110)$-$(2 \times m)$ surface reconstructions are predominantly composed of octahedrally coordinated TiO_6 units and in experimental observations include at least one Sr atom per unit cell.[15,21]

We started from the basis of our previous results on a Ti-poor reconstruction of $SrTiO_3(110)$, namely the (4×1) (see Fig. 1a).[31] We constructed a database of 495 structures, re-evaluated using VASP[43] with the r^{2}SCAN functional[44] and trained a ten-member committee based on the descriptor-based NeuralIL architecture.[3,35] In committees the uncertainty is approximated by training a set of models that vary by initialization seed, hyperparameters, architecture, or training data, and monitoring their disagreement on a prediction to obtain the model variance. The majority of computational cost incurred when training a descriptor-based model can be attributed to the calculation of the descriptors and the associated vector-Jacobian product operator. NeuralIL enables a particularly efficient committee implementation by reusing these elements for all members, so that committees needed for uncertainty estimation can be trained with a negligible performance penalty.[35]

We then generated CMA-ES trajectories for the (2×2), (2×3)a and (2×3)b recon-

structures. The CMA-ES samples a population of λ individuals $\boldsymbol{x}_k^g$, $k = 1, .., \lambda$, for every generation g from the multivariate normal distribution

$$\boldsymbol{x}_k^{(g)} \sim \mathcal{N}\left(\boldsymbol{m}^{(g-1)}, \left[\sigma^{(g-1)}\right]^2 \boldsymbol{C}^{(g-1)}\right), \tag{1}$$

with distribution mean $\boldsymbol{m}$, step size σ and covariance matrix $\boldsymbol{C}$. The population size and initial mean, $\boldsymbol{m}^{(0)}$, and step size, $\sigma^{(0)}$, are user-defined. We refer to the initial mean as the founder structure. Starting from founders that were variations of published structures,[21] we iteratively added data using the committee uncertainty estimate aggregated structure-wise[35]

$$s = \frac{1}{3N}\sum_j^N \sum_{k \in x,y,z} s_j^k, \tag{2}$$

to identify structures that should be added to the training data. Here, N is the number of atoms and s_j^k the committee standard deviation of the k-th component of the force on atom j. In total, 519 (2×2) and 775 (2×3) training structures were generated during this process. The dataset was then refined by incorporating 141 (5×1) and a further 272 (4×1) structures from Ref. 31 into the training data in order to reinforce performance on $SrTiO_3(110)$-($n \times 1$) structures.

To illustrate the variation in the training data, Fig. 2 displays a 2D projection of the spherical Bessel descriptors of the local environments of Sr atoms using the uniform manifold approximation and projection for dimension reduction (UMAP) method for dimension reduction.[45] The background shows the distribution of all $SrTiO_3(110)$ data from the final dataset through hexagonal binning. The foreground of subplots (a)-(c) depicts the local Sr environments of the individual ($n \times 1$), (2×2) and (2×3) data sets, with the colors indicating the distance of each Sr atom from the center of the surface slab. It can be seen how the data from each reconstruction used for the initial dataset contributes their own distinct environments. Not surprisingly, the Sr in the (2×3) overlayer reconstructions, depicted as green points in the top left of Fig. 2(c), is particularly distinctive, since it did not occur in
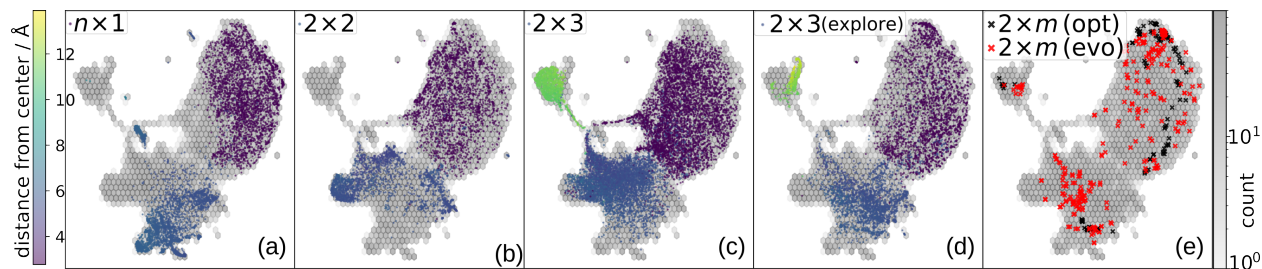
Figure 2: A two-dimensional UMAP representation of the spherical Bessel descriptors of the local environments of Sr atoms. The background of all plots displays the training data as fitted utilizing a log-log hexbin approach, with darker shading indicating higher data density per bin (right color bar). In the foreground of the first four columns, colored dots depict the local environments of Sr atoms corresponding to the structures labeled $(n \times 1)$, (2×2), (2×3) and "(2×3) (explore)", respectively. Here, the colors indicate each atom's distance from the center of the surface slab (left color bar). Column (e) features the local Sr descriptors of geometry-optimized $(2 \times m)$ results (including $c(2 \times 6)$, $(2 \times 4)c$, $c(2 \times 8)$, $(2 \times 4)d$, $(2 \times 4)f$, $(2 \times 5)b$ and $(2 \times 5)c$ projected on the same 2D UMAP background as black crosses. The red crosses in the same subplot depict the same for randomly chosen individuals from earlier generations of $(2 \times 4)f$ evolution runs, including generations 10, 25, and 50.

the $(n \times 1)$, (2×2) training data.

Exploration-based active learning

Using the 2226 structures in the initial training database, we trained a five-member committee using the equivariant message-passing neural network framework MACE.[4] MACE provides significantly improved accuracy and transferability and is more data-efficient than NeuralIL due to its equivariant architecture and custom-learned atomic representations. The mean absolute error in the force components, f_{MAE}, for the (4×1), (2×2) and (2×3) sets decreased by a factor of 2.5 when moving from NeuralIL to MACE with the same training data. Notably, the force uncertainty estimates obtained from MACE and NeuralIL committees, Eq. (2), exhibit a strong correlations for all highly uncertain configurations (see Fig. S3 of the SI). This underscores the efficiency of constructing the initial database using uncertainties derived from the NeuralIL committee. The initial MACE model demonstrated strong performance on test data and could reliably be applied to investigate $(n \times 1)$ and (2×2) structures using the CMA-ES with relative large population sizes, $\lambda = 100$, and

7

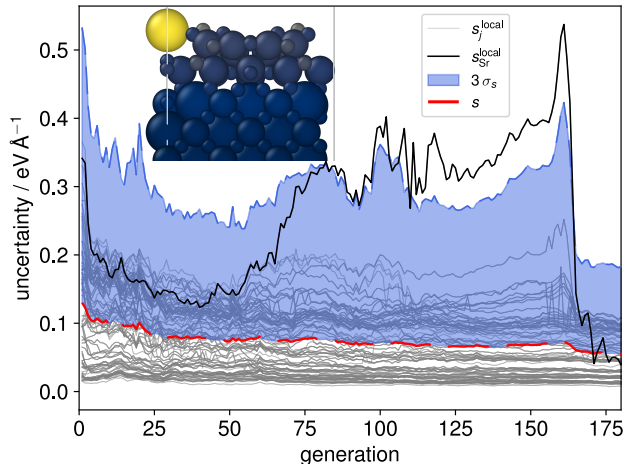initial step sizes, $\sigma^{(0)} \in [0.1, 0.35]$.

Figure 3: Spatially resolved uncertainty of a CMA-ES trajectory of a mirror-symmetric $SrTiO_3(110)$-(2×3) structure. The gray lines show the locally aggregated uncertainty s_j^{local} of each atom. The mean of all local uncertainties, i.e. the global structure uncertainty s, is depicted as a dashed red line, with three times their standard deviation σ_s shaded in blue. The local uncertainty associated with the overlayer Sr atom is highlighted in black. The inset shows a structure at generation 160 with the atoms colored according to the local uncertainty estimate. The color scale ranges from dark-blue (lowest) to yellow (highest local uncertainty).

We then performed exploratory CMA-ES searches on the (2×3) surface with population size $\lambda = 100$, and varying the initial step size in the range of $\sigma^{(0)} \in [0.1, 0.5]$. To expand the search space, we developed a more generic founder structure (pictured in Fig. S7 of the SI), rather than relying on published findings. From these searches, we identified the new $SrTiO_3(110)$-(2×3)c reconstruction, Fig. 1(c). A key feature of this structure is the alignment of the overlayer Sr atoms relative to the topmost TiO_x rows. A comparison between the geometry-optimized (2×3)b and (2×3)c systems reveals that (2×3)c has a lower energy, with a difference of ΔE=160 meV per (1×1) unit cell, using VASP for geometry optimization.

While two of the 35 initial CMA-ES searches produced the new stable configuration, a majority of these evolutionary searches were found to be prone to instability, specifically to the expulsion of an Sr atom. Although problematic structures could be identified manually, an active learning procedure needs to be able to identify and incorporate such structures

8

into the training data based on computed quantities such as model uncertainties. Since this behaviour was not reflected in the aggregated structure uncertainty as defined in Eq. (2), we utilized spatially resolved atomic uncertainties.[38] These are obtained by aggregating over neighboring atoms within a cutoff radius (in the following set to 4 Å) instead of over the entire structure

$$s_j^{\text{local}} = \frac{1}{3N_j} \sum_n^{N_j} \sum_{k \in x,y,z} s_n^k, \tag{3}$$

for atom j with N_j neighbors, and have been shown to exhibit a clear correlation with the local prediction error.[38]

The local uncertainties, Eq. (3), clearly identified the misinterpretation of unphysical local structures which led to escalating errors during the evolution and are thus a reliable indicator for atoms being expelled from the surface. A visual representation of the evolution of local and global uncertainty within a CMA-ES run is given in Fig. 3. The solid black line tracks the local uncertainty associated with the single Sr atom in the overlayer. Notably, $s_{\text{Sr}}^{\text{local}}$ begins to increase after generation 70 and exceeds three times the standard deviation of the local uncertainties ($3\,\sigma_s$) after generation 90, while the global structure uncertainty s, Eq. (2), indicated by a dashed red line, does not reflect this increase. This behavior is further illustrated by the atomic structure shown in the inset: at generation 160 even the configuration with the lowest energy features a bright yellow sphere, indicating the high local uncertainty in the force estimate for the Sr atom. In an additional AL step we then identified trajectories where the local uncertainty associated with at least one atom j exceeded three standard deviations of all local uncertainties ($s_j^{\text{local}} > 3\,\sigma_s$). The rise in local uncertainty corresponds to environments that the model is increasingly uncertain about but which are localized enough for them to have a low weight in the globally aggregated uncertainty, Eq. (2). Once an atom is separated from the rest by more than the cutoff radius of the underlying MLFF model, its contribution to the energy and forces, and thus also to the local and global uncertainty, becomes zero.

We randomly sampled structures from 40 CMA-ES evolution trajectories, with 32 of these

structures exhibiting similar local uncertainty behaviour as shown in Fig. 3. The sampling was performed uniformly but was restricted to intact surface slabs, meaning that generations following Sr expulsion were excluded. The 2D UMAP of the local Sr descriptors within these structures is shown in Fig. 2(d), highlighting the added diversity that was achieved. With these additional 392 structures, the full training set consisted of 2618 configurations. This was used to train the final MACE model which was utilized for all further CMA-ES runs. The complete database and trained model are made available on Zenodo.[46]
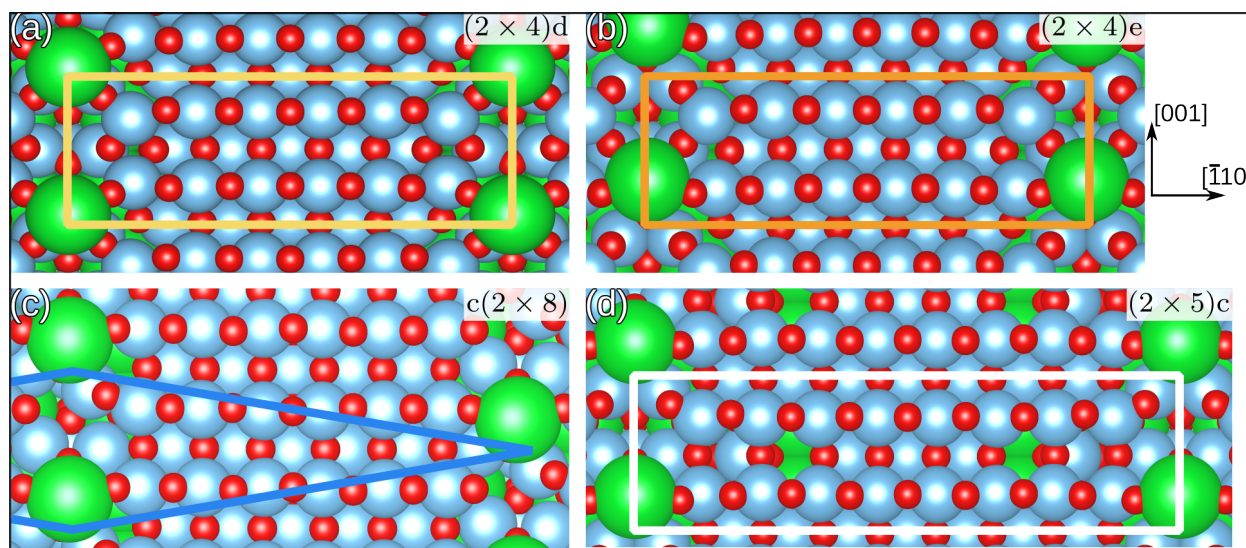

Figure 4: Top view of $SrTiO_3(110)$ overlayer candidates with (2×4) and (2×5) bulk periodicity. The orange and white rectangles and blue rhombus indicate (parts of) the respective unit cells.

Structure search

The model described above enabled us to perform a large number of structure searches for $SrTiO_3(110)$-$(2 \times m)$, $m \in \{3, 4, 5\}$, with initial step sizes in the range of $\sigma^{(0)} \in [0.1, 0.5]$. The choice of population size λ strongly influences the stability of the evolution trajectories, especially for such rough loss landscapes. Moreover, a larger population size increases the likelihood of identifying the most stable structure, rather than other stable structures nearby on the loss surface. Because of this trade-off, we performed the same searches with population

sizes between 25 and 100, as detailed in the Methods section.

The UMAP in Fig. 2(e) illustrates the variety of local Sr environments encountered in randomly selected structures chosen from early generations (10, 25 and 50) along these trajectories (red crosses). In comparison, the local environments in geometry-optimized structures of different unit cell sizes are clearly more uniform (black crosses). Throughout all CMA-ES searches, spatially resolved local uncertainty, along with the loss, served as an indicator for structure stability. Importantly, after adding the structures from the exploration-based active learning in the (2×3)cell, Fig. 2(d) ,to the training data, the MLFF learned to avoid regions leading to the previously observed overlayer instability. Fig. S4 of the SI shows uncertainty trajectories for (2×3), (2×4), and (2×5) runs, where no local uncertainty exceeds $3\sigma_s$. Of particular interest is the (2×3) trajectory, which still illustrates that the Sr environment is the most uncertain, but does not escalate anymore (compare to Fig. 3). Importantly, this demonstrates the transferability of the model when extrapolating to reconstruction with larger unit cells.

With this approach, we were able to discover the new candidate structures shown in Fig. 4, namely c(2×8) (blue), (2×4)d (yellow), (2×4)e (orange), and (2×5)c (white), which we compare to experiment in the following. All of these structures are available on Zenodo.[46]

Comparison to experiment

Figure 5 depicts a high-resolution STM image that illustrates how the preparation of Ti-rich surfaces results in a mixture of various surface structures. In this image, local symmetries with (2×4) (orange and yellow), (2×5) (white), and c(2×8) (blue) unit cells can be observed. In the STM images of the Ti-rich SrTiO$_3$(110) surfaces, the Sr and O atoms are visible as bright spots. In the cells shown in Fig. 5, the topmost TiO$_x$ rows (henceforth referred to as "TiO ridges" and experimentally imaged as bright spots) tend to be aligned with the Sr atoms. This feature is incompatible with the STM image obtained from the
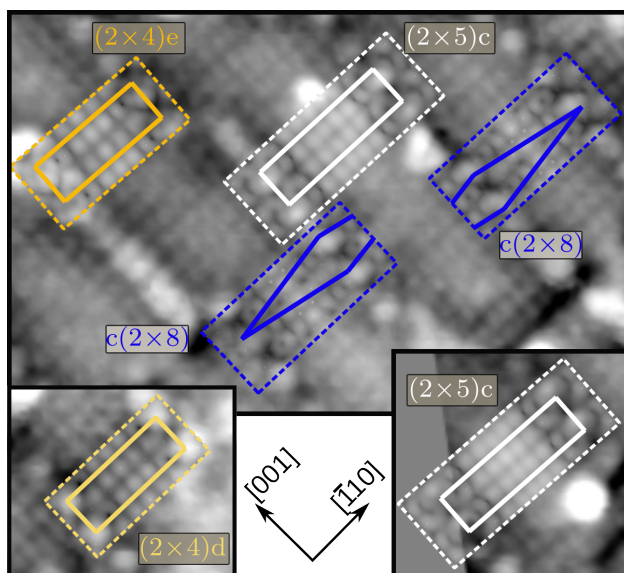
11

Figure 5: Different regions of the same STM measurement of Ti-rich SrTiO$_3$(110), showing (2×4) (orange and yellow) c(2×8) (blue) and (2×5) (white) unit cells. The colored dashed lines mark the border of simulated images, overlayed with 50% transparency, colored solid lines represent the unit cells. The same figure without overlay and also with fully opaque simulation images, as well as the full experimental image are part of the SI. Imaging parameters: $V_{\text{sample bias}} = +1.8\,\text{V}$, $I = 0.04\,\text{nA}$. Simulated images were created using the Tersoff-Hamann approximation.[47]

published (2×5)b structure,[21] where the TiO ridges are offset with respect to the Sr atoms.

Founder structures for investigating SrTiO$_3$(110)-(2×4) and (2×5) cells were created as described in Section S3 of the SI. In short, they were generated by varying initial atom positions and adjusting the stoichiometry (addition or removal of TiO$_2$ units). Details regarding the evolutionary searches, including the number of runs, population sizes λ, and step sizes σ are summarized in the Methods section. All newly proposed structures were tested by comparing the corresponding simulated STM images with the experimental data in Fig. 5. Important criteria for matching were the position of the Sr adatoms and their relative alignment to the TiO ridges.

For (2×5) systems, the initial placement of "TiO$_2$ vacancies" resulted in distinct founders, with the vacancies positioned either in-line or out-of-line relative to the overlayer Sr in the $[\bar{1}10]$ direction. All sensible configurations resulting from these founders yielded significantly higher energies than the SrTiO$_3$(110)-(2×5)b from Ref. 21. However, an alternative candi-

12

date structure, (2×5)c (see Fig. 4), could be identified due to its distinct features. There, in contrast to (2×5)b, the overlayer Sr atom is aligned with a TiO ridge rather than being offset. While the energy difference between the two is $\Delta E = 208$ meV per (1×1) unit cell in favor of (2×5)b, the new (2×5)c clearly fits regions of the heterogeneous surface as shown in Fig. 5.

The investigation of $SrTiO_3(110)$-(2×4) identified two stable surface structures, labeled (2×4)d and (2×4)e, both shown in Fig. 4. Although the difference in DFT energies between them is vanishingly small - only 2 meV per (1×1) unit cell in favor of (2×4)d - the arrangement of the overlayer atoms is distinct. The most noticeable differences include the relative position of the overlayer Sr atom with respect to the TiO ridges and the resulting positional changes. Additionally, the centered unit cell c(2×8) was found as a candidate structure for explaining regions on the STM measurement showing a shift between Sr positions.

The newly proposed structures c(2×8), (2×4)d, (2×4)e, and (2×5)c thus provide previously missing atomistic models for the different regions observed with STM on the heterogeneous surface.

Summary and conclusions

We successfully integrated neural-network force fields with the covariance matrix adaptation evolution strategy to develop an accurate and transferable machine-learned force field suitable for the exploration of Ti-rich $SrTiO_3(110)$ surface reconstructions. The required training data were generated through an active learning workflow, which involved repeatedly performing CMA-ES runs on $SrTiO_3(110)$-(2×2) and (2×3) founder structures to gather uncertain and diverse data. During this process, NeuralIL committees were utilized for energy evaluation and uncertainty estimation. The collected data was then used to train a MACE model suitable for production runs.

To fine-tune the training data in a further AL step, and thereby enhance model perfor-

mance, we employed spatially resolved uncertainty estimation to identify underrepresented local environments which global uncertainty measures had failed to resolve. The resulting MLFF, $MACE_{full}$, was trained on 2618 structures spanning $SrTiO_3(110)$-$(n \times m)$, $n \in \{4, 5\}$, $m \in \{2, 3\}$.

We successfully identified two not previously reported candidates for stable (2×3) reconstructions. These structures were then used to extrapolate to (2×4) and (2×5) founder structures for evolutionary exploration. With this approach, we found new stable candidate structures for $SrTiO_3(110)$-(2×4) and (2×5), explaining different experimentally observed regions of the heterogeneous Ti-rich surface. This method could be extended to other multi-element oxides featuring complex, composition-related, and possibly coexisting surface reconstructions characterized by large unit cells.

Methods

CMA-ES

We applied CLINAMEN2,[48] a functional-style Python framework that interfaces to different codes for loss evaluation in a straightforward manner, to perform the covariance matrix adaptation evolution strategy (CMA-ES)[42] for all structure searches in this study.

Surface slabs were set up as illustrated in Ref. 31, with the atomic positions in Cartesian coordinates serving as the degrees of freedom, i.e., the variables adjustable by the CMA-ES. For all system sizes an anchor region of fixed atom positions was defined at the center of each slab, consisting of bulk-like layers that remained unchanged. Opposite sides of all slabs were made symmetric, allowing for the manipulation of only the overlayer- and attachment-layer atoms. Further symmetry elements (e.g. mirror planes) were leveraged where feasible to drastically reduce the number of degrees of freedom in larger unit cells.

14

DFT

We used VASP[43] version 6.2.0 with the r²SCAN functional[44] for all ab-initio calculations in this study, including single-shot structure evaluations for training and test data and geometry optimization of low-energy candidate structures. The energy cutoff was set to 440 eV and the width of Gaussian smearing to 0.02 eV. To ensure compatibility of DFT energies and forces calculated for different system sizes we utilized the optimized k-point grid generator by Wang et al.[49]

Machine-learned force fields

All NeuralIL models in this work used $r_{cut} = 4.0$ Å and $n_{max} = 5$, with ResNet core widths set to [256, 128, 64, 32, 32, 32, 16]. Training on forces was run for only 101 epochs due to the replacement of the standard Adam optimizer with the versatile learned optimizer VeLO,[50] drastically reducing the number of epochs needed for convergence by orders of magnitude.[35]

With the majority of hyperparameters set to default values, MACE trainings were performed with a cutoff radius $r_{max} = 4.0$ Å and two hidden layers set to 128 channels for scalar and vector properties each. The maximum number of epochs was set to 1200 with an early stopping patience of 50, and energy and force weights of 1 and 100, respectively. Afterwards, training was run for an additional 300 epochs with an increased energy weight of 1000 and an unchanged force weight.

Evolution details

In total, approximately 3000 exploratory CMA-ES runs were performed on various system sizes and founder structures. For each founder, runs were started for different random seeds to leverage the stochasticity of the method. Population sizes were varied between $\lambda \in \{25, 35, 50, 100\}$, with the choice of step size σ depending on symmetry. Whenever mirror symmetry was enforced, $\sigma^{(0)}$ was capped at 0.35 Å, while evolutionary searches without

15

symmetry were performed for step sizes up to $0.5\,\text{Å}$. The lower limit for $\sigma^{(0)}$ was $0.1\,\text{Å}$ for all cases.

The computation of one CMA-ES trajectory starting from a founder containing 450 atoms and running for up to 1000 generations, with population size $\lambda = 100$, required only between one and three hours on one NVIDIA A40 GPU with $46\,\text{GiB}$ memory when utilizing $\text{MACE}_{\text{full}}$, depending on early stopping. For that reason, it was possible to freely explore various founders to then select highlights for further investigation using DFT.

Experimental methods

$SrTiO_3(110)$ single crystals (CrysTec GmbH, 0.5 wt. % Nb_2O_5, $5 \times 5 \times 0.5\,\text{mm}^3$, one-side polished, miscut less than $0.3°$) were prepared *ex situ* by sonication in heated neutral detergent (3 % Extran® MA02 diluted in ultrapure water, $2 \times 20\,\text{min}$) and ultrapure water (milli-Q™, $10\,\text{min}$). Subsequent boiling for $10\,\text{min}$ in milli-Q™ water removed commonly observed CaO contamination. The samples were then mounted on Omicron-style, HNO_3-cleaned Nicrofer® sample plates with Nicrofer® clips, and inserted in a UHV setup comprising three interconnected chambers: (i) a preparation chamber (base pressure below $10^{-10}\,\text{mbar}$) equipped with sputtering–annealing facilities and an evaporator for Sr deposition; (ii) an analysis chamber (base pressure below $5 \times 10^{-11}\,\text{mbar}$) equipped for STM (SPECS Aarhus STM 150), low-energy electron diffraction (LEED) (Omicron), and x-ray photoelectron spectroscopy (XPS) (nonmonochromatic dual-anode Mg/Al $K\alpha$ source, SPECS Phoibos 100 analyzer, normal emission); (iii) a pulsed-laser deposition (PLD) chamber (base pressure below $2 \times 10^{-9}\,\text{mbar}$).

After a few cycles of sputtering–annealing ($6 \times 10^{-6}\,\text{mbar}$ Ar, $1\,\text{keV}$, 5–$10\,\mu\text{A}$, $10\,\text{min}$, followed by $1\,\text{h}$ at $1000\,°\text{C}$, $6 \times 10^{-6}\,\text{mbar}$ O_2), the surface cleanliness was verified through XPS and STM. The surface stoichiometry was then adjusted via submonolayer deposition of Sr (via molecular-beam epitaxy)[51] or TiO_2 (via PLD).[52] The resulting surface periodicity was verified by LEED and STM. The surface presented in this work was obtained starting from a mixed $(4 - 5 \times 1)$ reconstruction. $1.4\,\text{ML}$ Ti was deposited in PLD by keeping the

16

sample at $580\,°C$ in a background oxygen pressure of $6 \times 10^{-6}\,$mbar O_2, followed by ramp down at $80\,°C\,min^{-1}$.

STM images were acquired in constant-current mode with homemade, electrochemically etched W tips. The tips were prepared *in situ* by Ar sputtering ($1\,\mu A$, $30\,min$). Voltage (up to $10\,V$) or current pulses (up to $10\,nA$) were applied while in tunneling contact to reshape the tip and improve resolution. Positive bias voltages correspond to tunneling into the empty states of the sample.

Data and Software Availability

The trained models, training and test data, and POSCAR files containing founders and results are available on Zenodo.[46]

Acknowledgement

Supporting Information Available

Additional figures comparing simulation to STM measurements and further details on uncertainty estimation. Moreover, the algorithm and figures explaining founder generation, and information on overall model performance.

References

(1) Behler, J.; Parrinello, M. Generalized Neural-Network Representation of High-Dimensional Potential-Energy Surfaces. *Phys. Rev. Lett.* **2007**, *98*, 146401, DOI: `10.1103/PhysRevLett.98.146401`.

(2) Schütt, K. T.; Sauceda, H. E.; Kindermans, P.-J.; Tkatchenko, A.; Müller, K.-R. SchNet – A Deep Learning Architecture for Molecules and Materials. *The Journal of Chemical Physics* **2018**, *148*, 241722, DOI: `10.1063/1.5019779`.

(3) Montes-Campos, H.; Carrete, J.; Bichelmaier, S.; Varela, L. M.; Madsen, G. K. H. A Differentiable Neural-Network Force Field for Ionic Liquids. *J. Chem. Inf. Model.* **2021**, *62*, 88–101, DOI: `10.1021/acs.jcim.1c01380`.

(4) Batatia, I.; Kovacs, D. P.; Simm, G.; Ortner, C.; Csányi, G. MACE: Higher Order Equivariant Message Passing Neural Networks for Fast and Accurate Force Fields. *Adv. Neural. Inf. Process. Syst.* **2022**, *35*, 11423–11436.

(5) Batzner, S.; Musaelian, A.; Sun, L.; Geiger, M.; Mailoa, J. P.; Kornbluth, M.; Molinari, N.; Smidt, T. E.; Kozinsky, B. E(3)-Equivariant Graph Neural Networks for Data-Efficient and Accurate Interatomic Potentials. *Nat Commun* **2022**, *13*, 2453, DOI: `10.1038/s41467-022-29939-5`.

(6) Liao, Y.-L.; Wood, B.; Das, A.; Smidt, T. EquiformerV2: Improved Equivariant Transformer for Scaling to Higher-Degree Representations. **2024**, DOI: `10.48550/arXiv:2312.04174`.

(7) Batatia, I. et al. A Foundation Model for Atomistic Materials Chemistry. **2024**, DOI: `10.48550/arXiv.2401.00096`.

(8) Maxson, T.; Szilvási, T. Transferable Water Potentials Using Equivariant Neural

Networks. *J. Phys. Chem. Lett.* **2024**, *15*, 3740–3747, DOI: `10.1021/acs.jpclett.4c00605`.

(9) Zhang, S.; Makoś, M. Z.; Jadrich, R. B.; Kraka, E.; Barros, K.; Nebgen, B. T.; Tretiak, S.; Isayev, O.; Lubbers, N.; Messerly, R. A.; Smith, J. S. Exploring the Frontiers of Condensed-Phase Chemistry with a General Reactive Machine Learning Potential. *Nat. Chem.* **2024**, *16*, 727–734, DOI: `10.1038/s41557-023-01427-3`.

(10) Spinelli, A.; Torija, M. A.; Liu, C.; Jan, C.; Leighton, C. Electronic Transport in Doped SrTiO$_3$: Conduction Mechanisms and Potential Applications. *Phys. Rev. B* **2010**, *81*, 155110, DOI: `10.1103/PhysRevB.81.155110`.

(11) Takahashi, K. S.; Gabay, M.; Jaccard, D.; Shibuya, K.; Ohnishi, T.; Lippmaa, M.; Triscone, J. M. Local Switching of Two-Dimensional Superconductivity Using the Ferroelectric Field Effect. *Nature* **2006**, *441*, 195, DOI: `10.1038/nature04731`.

(12) Wang, Z.; Zhong, Z.; Hao, X.; Gerhold, S.; Stöger, B.; Schmid, M.; Sánchez-Barriga, J.; Varykhalov, A.; Franchini, C.; Held, K.; Diebold, U. Anisotropic Two-Dimensional Electron Gas at SrTiO$_3$(110). *Proc. Natl. Acad. Sci. U. S. A.* **2014**, *111*, 3933, DOI: `10.1073/pnas.1318304111`.

(13) Dudy, L.; Sing, M.; Scheiderer, P.; Denlinger, J. D.; Schütz, P.; Gabel, J.; Buchwald, M.; Schlueter, C.; Lee, T.-L.; Claessen, R. In Situ Control of Separate Electronic Phases on SrTiO$_3$ Surfaces by Oxygen Dosing. *Adv. Mater.* **2016**, *28*, 7443, DOI: `10.1002/adma.201600046`.

(14) Shibuya, K.; Ohnishi, T.; Uozumi, T.; Sato, T.; Lippmaa, M.; Kawasaki, M.; Nakajima, K.; Chikyow, T.; Koinuma, H. Field-Effect Modulation of the Transport Properties of Nondoped SrTiO$_3$. *Appl. Phys. Lett.* **2006**, *88*, 212116, DOI: `10.1063/1.2207502`.

(15) Andersen, T. K.; Fong, D. D.; Marks, L. D. Pauling's Rules for Oxide Surfaces. *Surf. Sci. Rep.* **2018**, *73*, 213–232, DOI: `10.1016/j.surfrep.2018.08.001`.

(16) Tanaka, H.; Matsumoto, T.; Kawai, T. K. T.; Kawai, S. K. S. Surface Structure and Electronic Property of Reduced SrTiO3(100) Surface Observed by Scanning Tunneling Microscopy/Spectroscopy. *Jpn. J. Appl. Phys.* **1993**, *32*, 1405, DOI: `10.1143/JJAP.32.1405`.

(17) Kubo, T.; Nozoye, H. Surface Structure of SrTiO3(100). *Surf. Sci.* **2003**, *542*, 177–191, DOI: `https://doi.org/10.1016/S0039-6028(03)00998-1`.

(18) Enterkin, J. A.; Subramanian, A. K.; Russell, B. C.; Castell, M. R.; Poeppelmeier, K. R.; Marks, L. D. A Homologous Series of Structures on the Surface of SrTiO3(110). *Nat Mater* **2010**, *9*, 245–248, DOI: `10.1038/nmat2636`.

(19) Kienzle, D. M.; Becerra-Toledo, A. E.; Marks, L. D. Vacant-Site Octahedral Tilings on $SrTiO_3(001)$, the $(\sqrt{13}\times\sqrt{13})$R33.7° Surface, and Related Structures. *Phys. Rev. Lett.* **2011**, *106*, 176102, DOI: `10.1103/PhysRevLett.106.176102`.

(20) Gerhold, S.; Wang, Z.; Schmid, M.; Diebold, U. Stoichiometry-Driven Switching between Surface Reconstructions on $SrTiO_3(001)$. *Surf. Sci.* **2014**, *621*, L1, DOI: `10.1016/j.susc.2013.10.015`.

(21) Wang, Z.; Loon, A.; Subramanian, A.; Gerhold, S.; McDermott, E.; Enterkin, J. A.; Hieckel, M.; Russell, B. C.; Green, R. J.; Moewes, A.; Guo, J.; Blaha, P.; Castell, M. R.; Diebold, U.; Marks, L. D. Transition from Reconstruction Toward Thin Film on the (110) Surface of Strontium Titanate. *Nano Lett.* **2016**, *16*, 2407–2412, DOI: `10.1021/acs.nanolett.5b05211`.

(22) Riva, M.; Franceschi, G.; Lu, Q.; Schmid, M.; Yildiz, B.; Diebold, U. Pushing the Detection of Cation Nonstoichiometry to the Limit. *Phys. Rev. Mater.* **2019**, *3*, 043802, DOI: `10.1103/PhysRevMaterials.3.043802`.

(23) Pancotti, A.; Silva, J.; de Siervo, A.; Landers, R.; Nascente, P. Surface Structure Characterization of a $(\sqrt{5} \times \sqrt{5})$-R26.6° Reconstruction of Strontium Titanate (001) by X-ray Photoelectron Diffraction. *Surf. Sci.* **2022**, *715*, 121937, DOI: `https://doi.org/10.1016/j.susc.2021.121937`.

(24) Marks, L. D.; Chiaramonti, A. N.; Rahman, S. U.; Castell, M. R. Transition from Order to Configurational Disorder for Surface Reconstructions on SrTiO$_3$(111). *Phys. Rev. Lett.* **2015**, *114*, 226101, DOI: `10.1103/PhysRevLett.114.226101`.

(25) Morales, E. H.; Martirez, J. M. P.; Saidi, W. A.; Rappe, A. M.; Bonnell, D. A. Coexisting Surface Phases and Coherent One-Dimensional Interfaces on BaTiO3(001). *ACS Nano* **2014**, *8*, 4465–4473, DOI: `10.1021/nn501759g`.

(26) Franceschi, G.; Schmid, M.; Diebold, U.; Riva, M. Atomically Resolved Surface Phases of La$_{0.8}$Sr$_{0.2}$MnO$_3$(110) Thin Films. *J. Mater. Chem. A* **2020**, *8*, 22947–22961, DOI: `10.1039/D0TA07032G`.

(27) Andersen, M. Machine Learning Speeds up Search for Surface Structure. *Nat. Comput. Sci.* **2023**, *3*, 1009–1010, DOI: `10.1038/s43588-023-00575-3`.

(28) Bisbo, M. K.; Hammer, B. Global Optimization of Atomic Structure Enhanced by Machine Learning. *Phys. Rev. B* **2022**, *105*, 245404, DOI: `10.1103/PhysRevB.105.245404`.

(29) Du, X.; Damewood, J. K.; Lunger, J. R.; Millan, R.; Yildiz, B.; Li, L.; Gómez-Bombarelli, R. Machine-Learning-Accelerated Simulations to Enable Automatic Surface Reconstruction. *Nat Comput Sci* **2023**, *3*, 1034–1044, DOI: `10.1038/s43588-023-00571-7`.

(30) Timmermann, J.; Kraushofer, F.; Resch, N.; Li, P.; Wang, Y.; Mao, Z.; Riva, M.; Lee, Y.; Staacke, C.; Schmid, M.; Scheurer, C.; Parkinson, G. S.; Diebold, U.; Reuter, K.

IrO_{2} Surface Complexions Identified Through Machine Learning and Surface Investigations. *Phys Rev Lett* **2020**, *125*, 206101, DOI: `10.1103/PhysRevLett.125.206101`.

(31) Wanzenböck, R.; Arrigoni, M.; Bichelmaier, S.; Buchner, F.; Carrete, J.; Madsen, G. K. H. Neural-Network-Backed Evolutionary Search for SrTiO3(110) Surface Reconstructions. *Digit. Discov.* **2022**, *1*, 703–710, DOI: `10.1039/D2DD00072E`.

(32) Brix, F.; Verner Christiansen, M.-P.; Hammer, B. Cascading Symmetry Constraint during Machine Learning-Enabled Structural Search for Sulfur-Induced Cu(111)-(43×43) Surface Reconstruction. *J. Chem. Phys.* **2024**, *160*, 174107, DOI: `10.1063/5.0201421`.

(33) Balestriero, R.; Pesenti, J.; LeCun, Y. Learning in High Dimension Always Amounts to Extrapolation. **2021**, DOI: `10.48550/arXiv.2110.09485`.

(34) Kahle, L.; Zipoli, F. Quality of Uncertainty Estimates from Neural Network Potential Ensembles. *Phys. Rev. E* **2022**, *105*, 015311, DOI: `10.1103/PhysRevE.105.015311`.

(35) Carrete, J.; Montes-Campos, H.; Wanzenböck, R.; Heid, E.; Madsen, G. K. H. Deep Ensembles vs Committees for Uncertainty Estimation in Neural-Network Force Fields: Comparison and Application to Active Learning. *J. Chem. Phys.* **2023**, *158*, DOI: `10.1063/5.0146905`.

(36) Jørgensen, P. B.; Busk, J.; Winther, O.; Schmidt, M. N. Coherent Energy and Force Uncertainty in Deep Learning Force Fields. **2023**, DOI: `10.48550/arXiv:2312.04174`.

(37) Kellner, M.; Ceriotti, M. Uncertainty Quantification by Direct Propagation of Shallow Ensembles. **2024**, DOI: `10.48550/arXiv.2402.16621`.

(38) Heid, E.; Schörghuber, J.; Wanzenböck, R.; Madsen, G. K. H. Spatially Resolved Uncertainties for Machine Learning Potentials. **2024**, DOI: `10.26434/chemrxiv-2024-k27ps`.

(39) Lee, Y.; Timmermann, J.; Panosetti, C.; Scheurer, C.; Reuter, K. Staged Training of Machine-Learning Potentials from Small to Large Surface Unit Cells: Efficient Global Structure Determination of the RuO2(100)-c(2×2) Reconstruction and (410) Vicinal. *J. Phys. Chem. C* **2023**, *127*, 17599–17608, DOI: `10.1021/acs.jpcc.3c04049`.

(40) Slavensky, A. M.; Christiansen, M.-P. V.; Hammer, B. Generating Candidates in Global Optimization Algorithms Using Complementary Energy Landscapes. *The Journal of Chemical Physics* **2023**, *159*, 024123, DOI: `10.1063/5.0156218`.

(41) Smith, J. S.; Nebgen, B.; Lubbers, N.; Isayev, O.; Roitberg, A. E. Less Is More: Sampling Chemical Space with Active Learning. *J. Chem. Phys.* **2018**, *148*, 241733, DOI: `10.1063/1.5023802`.

(42) Hansen, N. The CMA Evolution Strategy: A Tutorial. **2016**, DOI: `10.48550/arXiv.1604.00772`.

(43) Kresse, G.; Furthmüller, J. Efficient Iterative Schemes for Ab Initio Total-Energy Calculations Using a Plane-Wave Basis Set. *Phys. Rev. B* **1996**, *54*, 11169–11186, DOI: `10.1103/PhysRevB.54.11169`.

(44) Furness, J. W.; Kaplan, A. D.; Ning, J.; Perdew, J. P.; Sun, J. Accurate and Numerically Efficient r2SCAN Meta-Generalized Gradient Approximation. *J. Phys. Chem. Lett.* **2020**, *11*, 8208– 8215, DOI: `10.1021/acs.jpclett.0c02405`.

(45) McInnes, L.; Healy, J.; Melville, J. UMAP: Uniform Manifold Approximation and Projection for Dimension Reduction. **2020**, DOI: `10.48550/arXiv.1802.03426`.

(46) Wanzenböck, R.; Heid, E.; Riva, M.; Franchesci, G.; Imre, A. M.; Carrete, J.; Diebold, U.; Madsen, G. K. H. Data for Machine-Learning-Backed Evolutionary Exploration of Ti-rich SrTiO3(110) Surface Reconstructions. 2024; `https://doi.org/10.5281/zenodo.12528626`.

(47) Tersoff, J.; Hamann, D. R. Theory and Application for the Scanning Tunneling Microscope. *Phys. Rev. Lett.* **1983**, *50*, 1998–2001, DOI: `10.1103/PhysRevLett.50.1998`.

(48) Wanzenböck, R.; Buchner, F.; Kovács, P.; Madsen, G. K. H.; Carrete, J. Clinamen2: Functional-style Evolutionary Optimization in Python for Atomistic Structure Searches. *Comput. Phys. Commun.* **2024**, *297*, 109065, DOI: `https://doi.org/10.1016/j.cpc.2023.109065`.

(49) Wang, Y.; Wisesa, P.; Balasubramanian, A.; Dwaraknath, S.; Mueller, T. Rapid Generation of Optimal Generalized Monkhorst-Pack Grids. *Comput. Mater. Sci.* **2021**, *187*, 110100, DOI: `https://doi.org/10.1016/j.commatsci.2020.110100`.

(50) Metz, L.; Harrison, J.; Freeman, C. D.; Merchant, A.; Beyer, L.; Bradbury, J.; Agrawal, N.; Poole, B.; Mordatch, I.; Roberts, A.; Sohl-Dickstein, J. VeLO: Training Versatile Learned Optimizers by Scaling Up. **2022**, DOI: `10.48550/arXiv.2211.09760`.

(51) Wang, Z.; Yang, F.; Zhang, Z.; Tang, Y.; Feng, J.; Wu, K.; Guo, Q.; Guo, J. Evolution of the Surface Structures on SrTiO3(110) Tuned by Ti or Sr Concentration. *Phys. Rev. B* **2011**, *83*, 155453, DOI: `10.1103/PhysRevB.83.155453`.

(52) Riva, M.; Kubicek, M.; Hao, X.; Franceschi, G.; Gerhold, S.; Schmid, M.; Hutter, H.; Fleig, J.; Franchini, C.; Yildiz, B.; Diebold, U. Influence of Surface Atomic Structure Demonstrated on Oxygen Incorporation Mechanism at a Model Perovskite Oxide. *Nat Commun* **2018**, *9*, 3710, DOI: `10.1038/s41467-018-05685-5`.